

ProSGNeRF: Progressive Dynamic Neural Scene Graph with Frequency Modulated Foundation Model in Urban Scenes

Tianchen Deng¹, Yanbo Wang¹, Yejia Liu¹, Chenpeng Su¹, Jingchuan Wang¹,
Hesheng Wang¹, Danwei Wang², Shao-Yuan Lo^{*3}, Weidong Chen^{*1}

¹Shanghai Jiao Tong University.

²Nanyang Technological University.

³National Taiwan University.

Abstract

Implicit neural representation has demonstrated promising results in 3D reconstruction on various scenes. However, existing approaches either struggle to model fast-moving objects or are incapable of handling large-scale camera ego-motions in urban environments. This leads to low-quality synthesized views of the large-scale urban scenes. In this paper, we aim to jointly solve the problems caused by large-scale scenes and fast-moving vehicles, which are more practical and challenging. To this end, we propose a progressive scene graph network architecture to learn the local scene representations of dynamic objects and global urban scenes. The progressive learning architecture dynamically allocates a new local scene graph trained on frames within a temporal window, with the window size automatically determined, allowing us to scale up the representation to arbitrarily large scenes. Besides, according to our observations, the training views of dynamic objects are relatively sparse according to rapid movements, which leads to a significant decline in reconstruction accuracy for dynamic objects. Therefore, we utilize a foundation model network to encode the latent code. Specifically, we leverage the generalization capability of the visual foundation model DINOv2 to extract appearance and shape codes, and train the network on a large-scale urban scene object dataset to enhance its prior modeling ability for handling sparse-view dynamic inputs. In parallel, we introduce a frequency-modulated module that regularizes the frequency spectrum of objects, thereby addressing the challenge of modeling sparse image inputs from a frequency-domain perspective. Experimental results demonstrate that our method achieves state-of-the-art view synthesis accuracy, object manipulation, and scene roaming ability in various scenes. The code will be open-sourced on <https://github.com/dtc11111/prosgnerf>.

Keywords: 3D Scene Reconstruction, Foundation Model, Neural Scene Graph, Large-scale Urban Scenes

1 Introduction

Scene reconstruction and view synthesis on urban scenes have significantly changed our lives, particularly in autonomous driving [10], city simulation, and virtual reality (VR) [52] and Augmented Reality (AR) [6]. The development of autonomous

driving requires substantial and accurate testing to ensure safe behavior when deployed in the real world. View synthesis and controllable simulation for driving scenes also enable the generation of corner cases, and safety-critical situations aid in validating and enhancing the safety of autonomous driving systems at a lower cost.

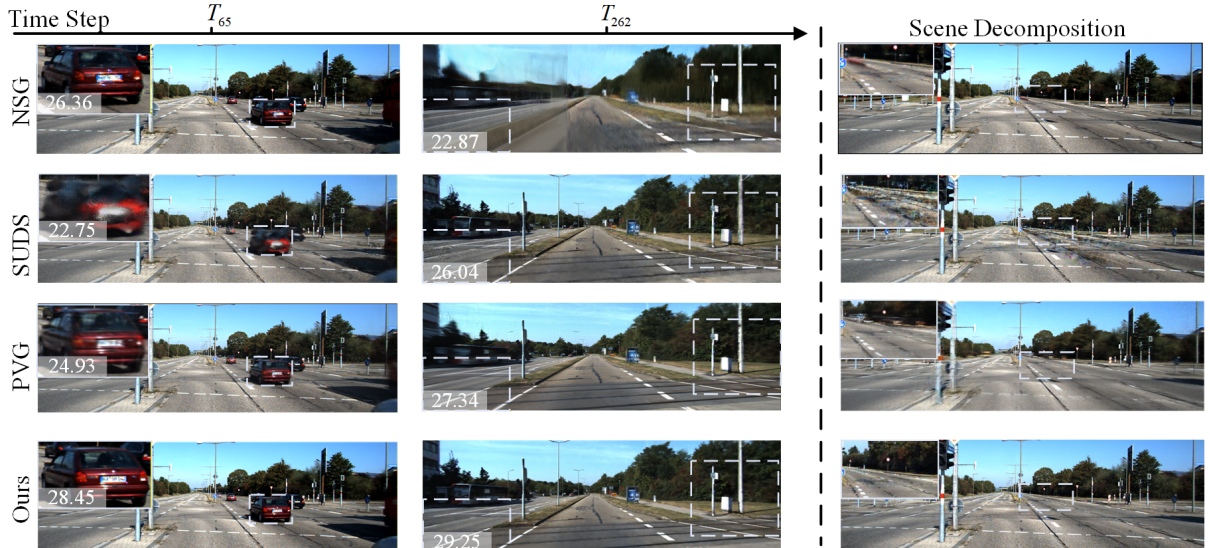


Fig. 1 Urban scene reconstruction and editing with ProSGNeRF. We show our view synthesis in different time steps (65,262) and scene decomposition results. Our approach significantly improves the view synthesis performance in real-world urban scenes containing multiple dynamic objects and large-scale camera ego-motion. We highlight and enlarge objects in the first column of images, providing the corresponding object PSNR in the top left corner. Scene PSNR is provided in the second column.

NeRF [29] is the most impressive method using implicit neural representation and has shown promising results for view synthesis on static and object-centric scenes. Some recent works improve the original NeRF and achieve large-scale urban scene reconstruction. Block-nerf [38] pre-divides the scene into multiple blocks with per-block update for virtual drive-through reconstruction. Mega-nerf [39] uses expanded octree architecture for large-scale photo-realistic fly-through scenarios. Bungeenerf [44] design a growing model with residual block structure for city-level scene reconstruction. [13, 28] focus on incremental scene representation, where multiple MLP modules are employed to model the entire scene, and the representations are fused through an online distillation strategy. NSG [32] introduces a scene graph architecture to represent the scene, while SUDS [40] factorizes the urban scene into three separate hash table data structures to efficiently encode static, dynamic, and far-field radiance fields. Mars [42] proposes a modular framework with instance-aware mask and separately with independent networks so that the static model the dynamic properties of instances and background. EmerNeRF [47] represents the scenes into static and dynamic fields.

It also uses the flow field to aggregate multi-frame features, improving the rendering precision of dynamic objects. Although existing methods have made improvements, they are still insufficient for real-world urban scenes. We summarize several core challenges for urban scene reconstruction: *a) multiple dynamic objects*. Existing algorithms have limitations in handling scenes with complex multiple-object motions. *b) insufficient scene representation capability*. Their representation capabilities are also limited with their single, global scene representation for the entire scenario. *c) sparse view input for dynamic objects*. In practical autonomous driving scenarios, observations of the same vehicle are limited to only a few frames (e.g. four or five images for a car), which leads to poor reconstruction performance for dynamic objects.

To this end, we propose ProSGNeRF for large-scale dynamic urban scene reconstruction and novel view synthesis. First, we propose a progressive neural scene graph architecture for learning the local scene representation with decoupled object transformations, background and far-field representation. The neural scene graph incorporates a progressive scheme that employs a temporal

window strategy to effectively address scalability, dividing the entire scene into multi-local scenes and dynamically initiating and maintaining local scene graphs. In each local scene graph, we incorporate multiresolution hash encoding into the background representation to better model low-level architectural details. Second, we design a frequency foundation model network to encode shape and appearance features for dynamic objects and regularize the frequency range of dynamic object information, which is efficient for sparse view input and enhances the representation of dynamic objects. We utilize the visual foundation model DINO V2 [5] to extract appearance and shape codes for dynamic objects with the prior information to enhance the reconstruction accuracy of dynamic objects. Third, the Segment Anything Model [22] has demonstrated its remarkable ability to revolutionize 2D segmentation. We leverage the promptable segmentation method to predict masks for dynamic objects and far-field scenarios, which can reduce the need for human annotation. We also use lidar projection supervision for geometry consistency. To validate our proposed framework, we evaluate the effectiveness of the method on different outdoor urban datasets, such as KITTI [18], VKITTI [3], Waymo [37], nuScenes [4] datasets, and do exhaustive evaluations and ablation experiments on these datasets. Our system demonstrates superior performance compared to existing methods that scene reconstruction on urban scenes. In summary, our contributions are shown as follows:

- We propose a novel editable neural scene reconstruction method, ProSGNeRF, which decomposes dynamic, background, and far-field into a progressively neural scene graph with decoupled object transformations and scene representations and also supports object manipulation and scene roaming.
- We propose a progressive neural scene graph representation architecture for the large-scale scenes, We dynamically instantiate local neural scene graphs with temporal sliding windows, enabling scalability to handle arbitrary large-scale scenes and long sequences.
- In each neural scene graph, the scene is decomposed into multiple dynamic objects and a background component. For background representation, we adopt a multiresolution hash

encoding strategy to effectively capture information at different frequency levels, enabling accurate modeling of both geometric structure and color appearance at fine spatial scales.

- Due to the sparse observation of objects in the urban scene, we design a frequency auto-encoder network with vision foundation model to efficiently encode shape and appearance features for the objects of interest and perform frequency modulation for sparse view inputs. In addition, to better train our vision foundation model, we construct a curated dataset consisting of hundreds of thousands of 2D images and corresponding 3D spatial information from the KITTI and Waymo datasets.
- We validate the effectiveness of our approach across multiple urban datasets, including KITTI and Virtual KITTI (vKITTI), Waymo datasets, which contain diverse scenarios with highly dynamic objects, as well as the large-scale Waymo dataset, which encompasses complex urban scenes with both static environments and dynamic objects such as vehicles and pedestrians.

2 Related Work

Recently, with the introduction and advancement of Neural Radiance Fields [29], a broad array of subsequent research has been inspired, building upon the original approach. We review the related work in the areas of implicit scene representations, dynamics, and large-scale scene representation.

2.1 Implicit Scene Representation

NeRF [29] is the most impressive work in view synthesis and 3D reconstruction. It proposes implicit representations to model scenes as functions, encoding the scene using a multi-layer perceptron (MLP). NeRF++ [49], Mip-nerf [1], and Mip-NeRF 360 [2] further improve the representation ability for unbounded environments. Those methods use the non-linear scene parameterization method to model unbounded scenes. [7] proposes a spherical radiance field (SRF) for efficient novel view synthesis in unbounded scenes. NeRF-W [27] incorporate per-image embeddings to model appearance variation of the outdoor scenes. NeRF-Der++ [20] and Surface-SOS [50] combine implicit scene representation with object detection method for semantic

3 Method

The pipeline of our system is shown in Fig. 2. We use a set of sequential RGB images $\{I_i\}_{i=1}^M$ with known pose $\{R|t\}$ as our input where M indicates the number of images. We construct the progressive neural scene graph with the instance mask from SAM and 3D bounding box from machine-predicted. The scene is decomposed into multi-local scene graphs with three branches: background, dynamic objects, and far-field. In the dynamic objects branch, we design a frequency auto-encoder to learn a normalized, object-centric representation whose embedding describes and disentangles shape, appearance, and pose. The decoder translates the features into occupancy and color information for given 3D points and viewing directions in object space. We also design lidar points projection geometry consistency in large-scale urban scenes.

3.1 Progressive Neural Scene Graph

All the existing dynamic NeRF systems have difficulties in large-scale urban scenes. They use a single, global representation for the entire environment, which limits their scene representation capacity. It causes problems when modeling large scenes: **a) a single model with fixed capacity cannot represent arbitrarily large-scale scenes.** **b) any misestimation has a global impact and might cause false reconstruction.**

To this end, we design a progressive neural scene graph to represent city-scale scenes with multi-dynamic objects. Instead of pre-dividing the scene with the camera poses, our method dynamically adjust local scene bounds during optimization, preventing the splitting of dynamic elements when applied to dynamic environments and improving the quality of reconstructing dynamic objects.

The scene graph SG, illustrated in Fig. 3, is composed of cameras, static nodes and a set of dynamic nodes which represent the dynamic components of the scene, including the object’s appearance, shape, and classes. The entire scene is decomposed into several local scene representations:

$$\{I_i, P_i\}_{i=1}^M \mapsto \{SG_{\theta_1}^1, SG_{\theta_2}^2, \dots, SG_{\theta_n}^n\} \mapsto \{c, \sigma\}$$

$$SG = \langle \mathcal{W}, C, L, F, E \rangle \quad (1)$$

P_i denotes the projection of the LiDAR point cloud at frame i . The root node of scene graph denoted as \mathcal{W} , C is a leaf node representing the camera in the global coordinate system and its intrinsic $K \in \mathbb{R}^{3 \times 3}$. L denotes the leaf node of scene graph (e.g. objects and background). F represents the neural networks for both static and dynamic nodes: $F = F_{\theta_{background}} \cup \{F_{\theta_1}, F_{\theta_2}, \dots, F_{\theta_c}\}$. E are edges that represent affine transformations from i to i' :

$$E = \{e_{i,i'} \in \{\emptyset, \mathbf{T}_{i \rightarrow i'}\}\},$$

$$\text{with } \mathbf{T}_{i \rightarrow i'} = \begin{bmatrix} \mathbf{R}_{i \rightarrow i'} & \mathbf{t}_{i \rightarrow i'} \\ \mathbf{0} & 1 \end{bmatrix}, \quad (2)$$

$$\mathbf{R}_{i \rightarrow i'} \in \text{SO}(3), \quad \mathbf{t}_{i \rightarrow i'} \in \text{SE}(3).$$

For all edges originating from the root node \mathcal{W} , we assign transformations between the global world space and the local objects with T . We compute the scaling factor S_i , assigned at edge e_i between an object node and its shared representation model F .

We present our progressive scheme in Algorithm 1. The algorithm describes a method for constructing a Progressive Neural Scene Graph that dynamically allocates a new local scene graph trained with frames within a temporal window, allowing us to scale up the representation to an arbitrarily large scene. Whenever the estimated camera pose trajectory reaches the bound of the current scene graph, we initialize the local representation with a local subset of frames, and then we progressively introduce subsequent frames to the optimization. For each frame, it optimizes the local neural scene graph and progresses to the next frame until a predefined condition is met. Each subset contains some overlapping images, essential for achieving consistent reconstructions in the global scene. When the limit for a local neural scene graph is reached, it initializes a new one, centered around the last pose, and continues the process until all frames are processed, contributing to the complete scene reconstruction. We further use inverse distance weight (IDW) fusion for all overlapping scene representations. Whenever the camera pose leaves the bound of the current scene representation, we stop optimizing previous ones (freeze the network parameters). At this point, we can reduce memory requirements and clear any supervising frames that are not needed anymore.

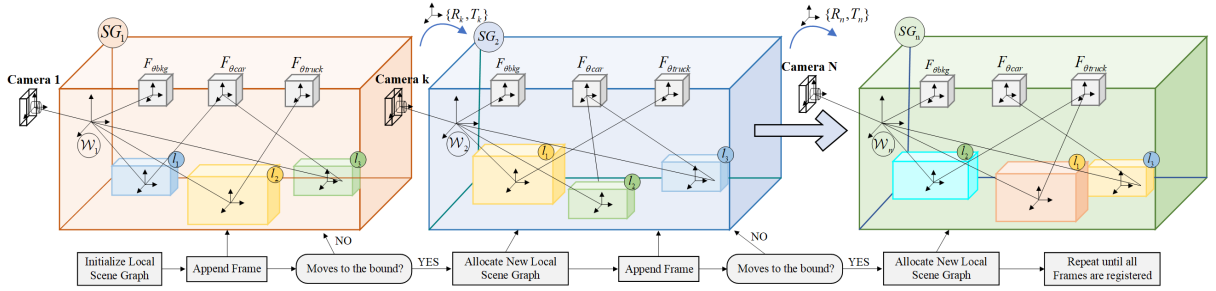


Fig. 3 The isometric view of the proposed progressive neural scene graph. This scene representation uses a progressive scheme that dynamically allocates a local neural scene graph (box) based on the camera pose. Adjacent local scene graphs have overlapping regions to maintain global consistency. The leaf nodes l are visualized as boxes with their local Cartesian coordinate axis. We also visualize the transformations and scaling between root and leaf coordinate frames using arrows with annotated transformation and scale matrices. The overall representation model is denoted as F_θ .

The progressive scene graph effectively addresses the camera’s large-scale ego-motion issue. It allows our scene reconstruction to scale to arbitrary sizes, significantly enhancing our capability to represent large-scale urban scenes.

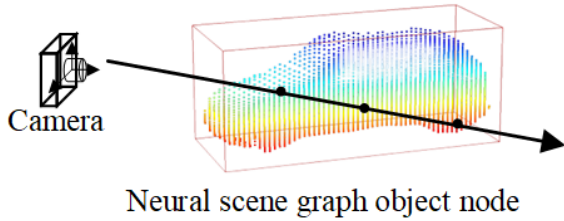


Fig. 4 Ray-Box Intersection. We use AABB ray-box sampling strategy. The boxes are now defined as an axis-aligned bounding box (AABB) with a minimum bound $[-1, -1, -1]$ and a maximum bound $[1, 1, 1]$.

3.2 Background Model

Our local scene graph includes a background representation node, as illustrated at the top of Fig. 2, which is responsible for modeling the static components of the environment. To more effectively capture scene texture, geometric details, and overall representation accuracy, we incorporate a multiresolution hash encoding method for background modeling. For a given input coordinate x , the surrounding voxels are identified across L resolution levels, and indices are assigned to their corner vertices by hashing the corresponding integer coordinates. The associated F dimensional feature vectors are then retrieved from the hash tables and linearly interpolated

Table 1 Background Model Architecture.

Background Model First Stage $F_{bckg,1}$		
Layer Name	Input	Size
Input	Local Position + Fourier	3 + 60
layer1	Fully Connected ReLU	256
layer2	Fully Connected ReLU	256
layer3	Fully Connected ReLU	256
layer4	Fully Connected ReLU + Skip	256
layer5	Fully Connected ReLU	256
layer6	Fully Connected ReLU	256
layer7	Fully Connected ReLU	256
PrevOut, Density	Fully Connected ReLU	256

Background Model Second Stage $F_{bckg,2}$		
Layer Name	Input	Size
Input	Direction + Fourier + PrevOut	3 + 24 + 256
second1	Fully Connected ReLU	256
second2	Fully Connected ReLU	256
second3	Fully Connected ReLU	256
RGB	Fully Connected ReLU	256

according to the relative position of x within each voxel. The interpolated features from all resolution levels are concatenated to form the final scene feature representation. The voxel resolutions are selected as a geometric progression ranging from the coarsest to the finest level, enabling efficient representation of both global structure and fine scale details. N_{min}, N_{max} :

$$N_l := \lfloor N_{min} \cdot b^l \rfloor, \quad (3)$$

$$b := \exp\left(\frac{\ln N_{max} - \ln N_{min}}{L - 1}\right)$$

Algorithm 1 Our Progressive Neural Scene Graph.

```
1:  $j \leftarrow 1$ ;          /* The first neural scene graph
   index*/
2:  $p \leftarrow 1$ ;      /* First camera pose index*/
3:  $q \leftarrow 1$ ;      /*Start with the first frames */
4:  $\{R, T\}_{p..q} \leftarrow 1$ ; /* Initialize poses as
   identity*/
5:  $\theta_j \leftarrow \text{InitializeSG}()$ ; /* Initialize the first
   local neural scene graph*/
6: while  $q < P$  do
7:   while  $\{R, t\}_j < \text{Bound}_j$  do
8:      $q \leftarrow q + 1$ ;
9:      $\{R, T\}_q \leftarrow \{R, T\}_{q-1}$ ; /* Append a pose
   at the end of the trajectory */
10:    Optimize( $\theta_j$ ); /* Optimize local neural
   scene graph */
11:   end
12:   if  $q < P$  then
13:      $j \leftarrow j + 1$ ; /* A new local neural scene
   graph index*/
14:      $\theta_j \leftarrow \text{InitializeSG}()$  /* Initialize a new
   local neural scene graph*/
15:      $t_j \leftarrow t_q$ ; /* Centered around the last
   pose*/
16:      $p \leftarrow p + n$ ; /* Stop considering the
   frames in last neural scene graph*/
17:   end if
18:   Repeat until all frames are registered.
19: end
```

N_{max} is chosen to match the finest detail in the training data. We use spatial hash function:

$$h(\mathbf{x}) = \left(\bigoplus_{i=1}^d x_i \pi_i \right) \bmod T \quad (4)$$

where \bigoplus denotes the bit-wise XOR operation and π_3 are large prime numbers. Effectively, this formulation applies an XOR operation to the outputs of per dimension linear congruential pseudo random permutations, thereby decorrelating the influence of individual dimensions on the resulting hash value. We choose $\pi_1 := 1$ for better cache coherence, $\pi_2 = 2654435761$, and $\pi_3 = 805459861$.

Then the background decoder maps a coordinate x , direction d and scene feature to its density

and color:

$$\begin{aligned} [\sigma(\mathbf{x}), \mathbf{z}] &= F_{\theta_{bk,1}}(\text{Hashenc}(\mathbf{x})) \\ \mathbf{c}(\mathbf{x}) &= F_{\theta_{bk,2}}(\gamma_d(\mathbf{d}), \mathbf{z}) \end{aligned} \quad (5)$$

We map the positional and directional inputs with $\gamma_x(\mathbf{x})$ and $\gamma_d(\mathbf{d})$ to higher frequency feature vectors to aid learning in the MLP model. There are two stages of the representation network: $F_{\theta_{bk,1}}$, $F_{\theta_{bk,2}}$. The output of the first MLP is the density and the latent code z , which encodes the geometry feature. We concatenate z with the directional feature $\gamma_d(\mathbf{d})$ as the input of the second background model. Thus, the background representation is implicitly stored in the weights.

Background Model Architecture For the background model, our first stage uses 8 fully-connected layers and the second stage uses 4 fully-connected layers. All layers have a hidden size of 256. Further architecture details are shown in Table. 1. The background representation model is implemented as a two staged multilayer perceptron. The inputs to the background model are exactly the same as NeRF. The inputs consist of a 3D point given in Cartesian coordinates $x = x, y, z$ to the first stage and a 3D direction with $d = d_x, d_y, d_z$ as input to the second. We use a Fourier feature mapping, which increases training speed for low dimensional features. The 3D location \mathbf{x} is mapped with a Fourier encoding at $k = 10$ frequencies for

$$\gamma(p) = [\dots, \sin(2^k \pi p), \cos(2^k \pi p), \dots] \text{ for } k = 0, \dots, K-1$$

resulting in a length 63 input vector to the first stage. 8 fully-connected layers form the first stage, that outputs a density value and an intermediate feature vector of size 256. The Fourier encoding for the direction uses 4 frequencies and the encoded vector is concatenated with the output feature vector $y(\mathbf{x})$ of size 256, resulting in a input vector of length 283 to the second stage. The 4 layer deep second stage outputs a color value.

3.3 Frequency Modulated Foundation Model

All existing NeRF methods have difficulties in multi-dynamic objects in urban scenes. The original NeRF method assumes the density σ is static, but both the density $\sigma(\mathbf{x})$ and color $\mathbf{c}(\mathbf{x})$ depend

on time (and video). SUDS [40] and Emernerf [47] use an optical flow method to differentiate dynamic objects from the background. However, their method cannot model dynamic objects effectively, resulting in blurred object portions and numerous artifacts in the rendered images. Furthermore, most of the dynamic objects only appear in a few observations. This setting starkly contrasts the majority of existing works that observe multiple views of the same object. To address this challenging problem, we propose a frequency auto-encoder in dynamic objects node to learn a normalized, object-centric high-level feature that describes and disentangles shape, appearance, and pose.

Auto-encoder is a type of neural network architecture used for unsupervised learning of efficient encodings of input data. They consist of an encoder network that maps the input to a latent code, and a decoder network that reconstructs the input from the code. We employ a vision foundation model as the encoder to extract accurate shape and appearance representations, benefiting from the strong priors learned through large scale pretraining. This design enables the proposed method to more effectively address the **sparse observation** challenges of dynamic objects in autonomous driving scenarios. The code is a compressed representation that encodes the most salient features of the data.

Dynamic Objects Node L_o . The architecture of our dynamic branch is shown in Fig. 2. We consider each rigid part that changes its position through the observation as the dynamics. Each dynamic object is represented by the frequency auto-encoder in the local space of its node L_o and position p_o . As the global location p_o of a dynamic object moves between frames, its scene representation also moves. We introduce local Object Coordinate Space (OCS) F_o , fixed and aligned with the object’s pose. The transformation in the the global frame F_W to F_o is given by

$$\mathbf{x}_o = \mathbf{S}_o \mathbf{T}_o^w \mathbf{x} \quad (6)$$

where \mathbf{S}_o is a matrix with the inverse length values in the middle. $s_o = [L_o, H_o, W_o]$ with $\mathbf{S}_o = \text{diag}(1/s_o)$. The scaling factor allows the network to learn size-independent representation. We share the weights of the network for the objects of the same class (such as cars, vans and trucks that were categorized during preprocessing.)

Shape and Appearance Encoder. For a input image I , we use the segment anything model and 3D object detector to get the 2D mask M and 3D

Table 2 Object Decoder Architecture.

Object Decoder Model		
Layer Name	Input	Size
density layer0	Agg.Block+ResnetBlockFC	128
density layer1	Agg.Block+ResnetBlockFC	128
density layer2	Agg.Block+ResnetBlockFC	128
density layer3	Agg.Block+ResnetBlockFC	128
density layer4	Agg.Block+ResnetBlockFC	128
density lin_out	Linear	1
color layer0	Agg.Block+ResnetBlockFC	128
color layer1	Agg.Block+ResnetBlockFC	128
color layer2	Agg.(+density_feats)+ResnetBlockFC	128
color layer3	Agg.(+query_cams)+ResnetBlockFC	128
color layer4	Agg.(+query_cams)+ResnetBlockFC	128
color lin_out	Linear	3

bounding box β . We encode the input images I depicting a given object of interest into a shape code \mathcal{S}_θ and an appearance code \mathcal{A}_θ via a neural network. Inspired by [30], we design a two-head output architecture with the vision foundation extractor for generating the shape code l_s and appearance code l_a , respectively.

We use the DINOv2 backbone to extract image features. The output tokens of the DINO model consist of both a class token and patch tokens. The class token primarily encodes high-level semantic information, which we map through a lightweight MLP to generate the shape code of the dynamic object. The patch tokens mainly capture local appearance cues such as color and texture. We apply a mean pooling operation over the patch tokens, followed by another lightweight MLP, to obtain the appearance code. The final latent representation comprises both the shape code and appearance code, each with 128 dimensions. Image inputs are scaled to a maximum of 320 pixels in each dimension, maintaining the original aspect ratio.

Shape and Appearance Decoder ϕ . The shape code l_s is fed to the shape decoder network ϕ_s which implicitly outputs an density value σ of the given coordinate x . Unlike the shape code decoder, the appearance code decoder ϕ_a uses both shape and appearance codes as the input with the positional and directional information. The appearance decoder also takes the dynamic object node information to perceive the object’s position better and implicitly outputs the RGB color c . In Tab. 2, we present architecture of object decoder.

Shape Decoder. The shape decoder is a MLP that is made of 5 ResNet blocks with hidden dimension 128. At each layer, we feed the previous feature map and the positional encoding of the query points. In order to match the dimensionality of the positional encoding with the hidden dimensions of the MLP, we apply a single linear layer and aggregate the output with the intermediate feature maps by a simple per-channel mean pooling.

Color Decoder. For decoding the color, we use a similar architecture as for the shape decoder: A MLP of 5 ResNet blocks with hidden dimensionality of 128 and additional linear aggregations for additional input: As for the shape decoder, we aggregate intermediate features with positional encodings by mean pooling. Furthermore, on the third layer we pass in the same way the output of the corresponding layer of the shape encoder. This enables the color decoder to incorporate estimated shape information. On the final two layers, we pass the view direction (encoded as 3-dimensional vector) to account for view-dependent effects.

Frequency Modulation. In real-world urban scenes, dynamic objects only appear in a few observations, which significantly differs from the settings of the original NeRF method. In sparse view settings, the Neural radiance field is prone to overfitting to these 2D images without explaining 3D geometry in a multi-view consistent way, leading to reconstruction failure. Prior work [48] has already demonstrated that this issue is presumably caused by the high-frequency feature of the input.

To this end, we further improve the feature-extracting foundation model with a frequency regularization method. The original method addressed the sparsity issue by utilizing a CNN network to encode the high-frequency features, which leads to the overfitting of high-frequency features. In this work, we use a linearly increasing frequency mask α to regulate the visible frequency spectrum of the position embedding function:

$$\begin{aligned} \gamma_L(\mathbf{x}) &= [\sin(\mathbf{x}), \cos(\mathbf{x}), \dots, \sin(2^{L-1}\mathbf{x}), \cos(2^{L-1}\mathbf{x})] \\ \gamma'_L(t, T; \mathbf{x}) &= \gamma_L(\mathbf{x}) \odot \alpha(t, T, L) \end{aligned} \quad (7)$$

where t and T are the current training iteration and the final iteration of frequency regularization. The mask α is increased based on the training

time:

$$\alpha_n(t, T, L) = \begin{cases} 1 & \text{if } n \leq \frac{t \cdot L}{T} + 3 \\ \frac{t \cdot L}{T} - \lfloor \frac{t \cdot L}{T} \rfloor & \text{if } \frac{t \cdot L}{T} + 3 < n \leq \frac{t \cdot L}{T} + 6 \\ 0 & \text{if } n > \frac{t \cdot L}{T} + 6 \end{cases} \quad (8)$$

α_n denotes the n -th value of α . Our method starts with raw inputs without positional encoding (low-frequency). Then, our mask linearly increases the visible frequency band as training progresses. Our frequency modulation avoids the unstable and susceptible high-frequency signals of those dynamic objects at the beginning of training. We gradually provide our network with high-frequency signals to avoid over-smoothness.

Frequency regularization restricts the high-frequency components of the neural network weights or activations during training. This prevents the model from overfitting to noisy high-frequency patterns in the data. It acts as a low-pass filter, smoothing the weight updates and forcing the model to learn more general, low-frequency representations, ultimately improving generalization. All the additional information related to scene graph dynamic objects nodes: the coordinate \mathbf{x} , direction $\theta\phi$, and object pose is embedded by our frequency encoding before they are put into the auto-encoder.

Our method addresses the reconstruction of dynamic objects from sparse observations, distinct from prior approaches such as FreeNeRF [48] that exclusively focus on static objects. Unlike FreeNeRF [48], which encodes only input points, our frequency auto-encoder architecture incorporates dynamic object poses, input points, and appearance and shape features from scene graph nodes. This adaptation significantly enhances the model’s capacity to handle complex dynamic scenes, surpassing the capabilities of the previous method. Our frequency auto-encoder significantly improves the scene representation of dynamic objects and achieves great performance in image reconstruction, novel view synthesis, and object editing.

3.4 Scene Graph Rendering

This section presents the differentiable rendering of our proposed progressive neural scene graph. Each local scene graph has a subset of overlapping images $I_k \in \mathbb{R}^{H \times W \times 3}$. The rays are generated from

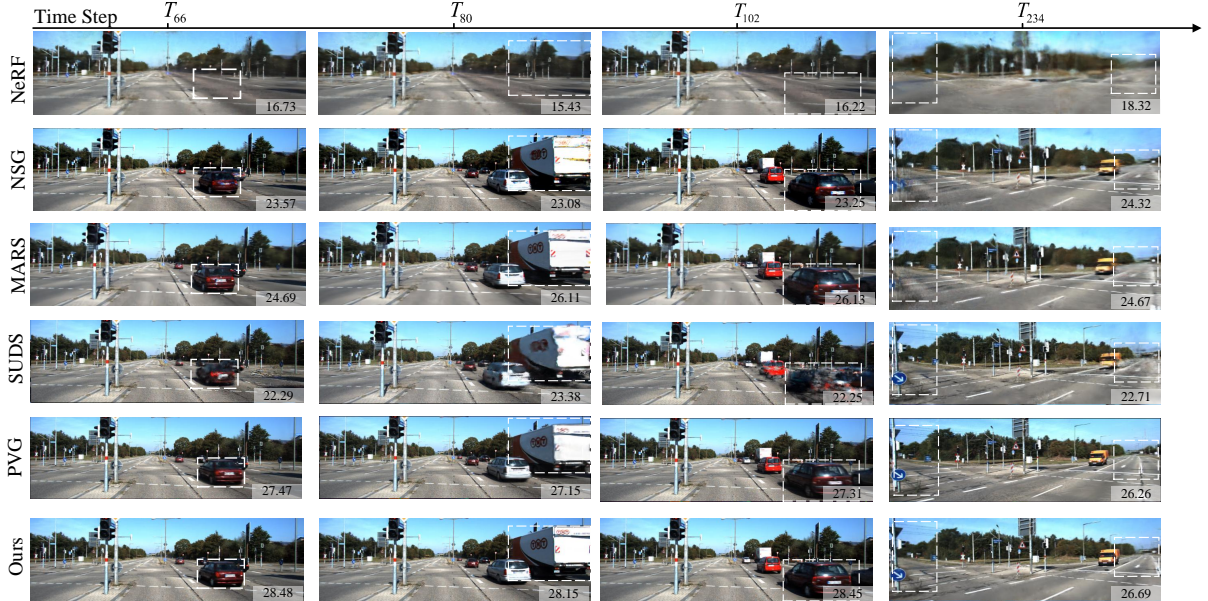


Fig. 5 Qualitative results on reconstruction and novel scene arrangements of a scene from the KITTI dataset [18] for NeRF [29], NSG [32], SUDS [40], MARS [42], PVG [8] and our method. From left to right, these images correspond to different timesteps captured in the dynamic scene. We place the PSNR values of each scene in the bottom right corner. NeRF and SUDS are limited in their ability to properly represent the dynamic parts of the scene. In contrast, our neural scene graph method achieves high-quality view synthesis results for both reconstruction and novel scene synthesis, regardless of scene dynamics.

Table 3 Image reconstruction and novel view synthesis results on the complete KITTI [18] dataset. We compare our method with others on PSNR, SSIM, and LPIPS metrics. For PSNR and SSIM, higher is better; for LPIPS, lower is better. Our method generates higher-quality rendering images both in image reconstruction and novel view synthesis.

Methods	Object Manipulation	Ego-Motion	Image Reconstruction KITTI [18]			KITTI - 75%			Novel View Synthesis KITTI - 50%			KITTI - 25%		
			PSNR \uparrow	SSIM \uparrow	LPIPS \downarrow	PSNR \uparrow	SSIM \uparrow	LPIPS \downarrow	PSNR \uparrow	SSIM \uparrow	LPIPS \downarrow	PSNR \uparrow	SSIM \uparrow	LPIPS \downarrow
NeRF [29]	\times	\times	16.98	0.509	0.524	16.81	0.509	0.524	16.64	0.504	0.535	16.55	0.498	0.544
NeRF+Time	\times	\times	24.18	0.677	0.237	22.05	0.612	0.262	21.90	0.602	0.239	20.17	0.591	0.253
NSG [32]	\checkmark	\times	26.66	0.857	0.071	25.25	0.801	0.089	24.81	0.786	0.105	22.31	0.752	0.134
SUDS [40]	\times	\checkmark	28.31	0.857	0.065	25.21	0.834	0.144	24.29	0.821	0.156	19.73	0.758	0.217
S-NeRF [45]	\times	\checkmark	19.25	0.664	0.193	18.71	0.606	0.352	18.31	0.598	0.361	17.93	0.586	0.365
3DGS [21]	\times	\checkmark	21.02	0.811	0.202	19.54	0.776	0.224	18.95	0.763	0.232	18.27	0.758	0.236
Mars [42]	\checkmark	\times	27.96	0.900	0.105	24.31	0.845	0.102	24.19	0.601	0.118	22.85	0.732	0.125
EmerNeRF [47]	\times	\checkmark	29.40	0.921	0.061	26.32	0.862	0.089	25.02	0.851	0.092	22.98	0.819	0.122
StreetGaussian [46]	\times	\checkmark	29.45	0.926	0.059	26.79	0.844	0.083	25.31	0.841	0.089	24.54	0.828	0.098
PVG [8]	\times	\checkmark	29.37	0.922	0.061	26.43	0.839	0.086	25.12	0.837	0.091	24.23	0.823	0.101
Ours	\checkmark	\checkmark	30.31	0.931	0.057	27.75	0.887	0.080	26.55	0.878	0.086	25.69	0.856	0.091

the images in scene graph SG with the camera intrinsic K and the transformation matrix T . We can determine a ray $r(t) = o + td$, whose origin is at the camera center of projection o , and ray direction r .

We use different sampling strategies for the background and dynamic objects. For the background, we use a multi-plane sampling strategy to increase efficiency. We define N_s planes parallel

to the image plane of the initial camera pose T_{wc} . The sample planes are within the near d_n and far planes d_f with stratified distribution. For a ray r , we calculate the intersections $t_{n=1}^{N_s}$ with each plane and get the sample point \mathbf{x}_{bkg} of the background. **Ray-Plane Intersection** Ray-Plane Intersection focuses on efficiently modeling static components using sparse planes. These planes are uniformly distributed along the scene’s depth,

Table 4 We report the PSNR, SSIM, and LPIPS metrics results on VKITTI2 [3] dataset. Our approach outperforms prior methods of reconstruction and novel view synthesis across all evaluation metrics.

Methods	Year	Image Reconstruction						Novel View Synthesis					
		VKITTI2 [18]			VKITTI2 - 75%			VKITTI2 - 50%			VKITTI2 - 25%		
		PSNR↑	SSIM↑	LPIPS↓	PSNR↑	SSIM↑	LPIPS↓	PSNR↑	SSIM↑	LPIPS↓	PSNR↑	SSIM↑	LPIPS↓
NeRF [29]	ECCV'20	17.63	0.525	0.511	17.11	0.513	0.514	16.94	0.517	0.521	16.65	0.504	0.537
NeRF + Time		24.54	0.683	0.235	22.59	0.619	0.252	22.15	0.612	0.261	21.82	0.615	0.233
NSG [32]	CVPR'21	27.18	0.894	0.092	25.45	0.886	0.094	24.95	0.794	0.101	23.49	0.758	0.105
SUDS [40]	CVPR'23	28.34	0.887	0.049	27.52	0.864	0.064	26.25	0.845	0.074	21.47	0.788	0.088
S-NeRF [45]	ICLR'23	20.53	0.874	0.181	19.46	0.646	0.342	19.11	0.604	0.354	18.43	0.591	0.359
StreetSurf [19]	Arxiv'23	24.89	0.839	0.242	23.88	0.785	0.273	22.79	0.776	0.289	21.59	0.746	0.303
3DGS [21]	TOG'24	22.34	0.868	0.179	21.42	0.657	0.339	21.11	0.624	0.347	20.84	0.863	0.329
Mars [42]	CICAI'23	30.26	0.925	0.083	29.79	0.917	0.088	29.63	0.916	0.087	27.01	0.877	0.104
Streetgaussian [46]	ECCV'24	31.37	0.928	0.081	30.08	0.922	0.084	30.03	0.910	0.089	28.13	0.905	0.099
PVG [8]	IJCV'26	31.69	0.931	0.077	30.45	0.925	0.080	30.15	0.914	0.086	28.45	0.910	0.095
Ours		32.42	0.938	0.075	31.58	0.935	0.079	30.95	0.931	0.084	29.69	0.927	0.088

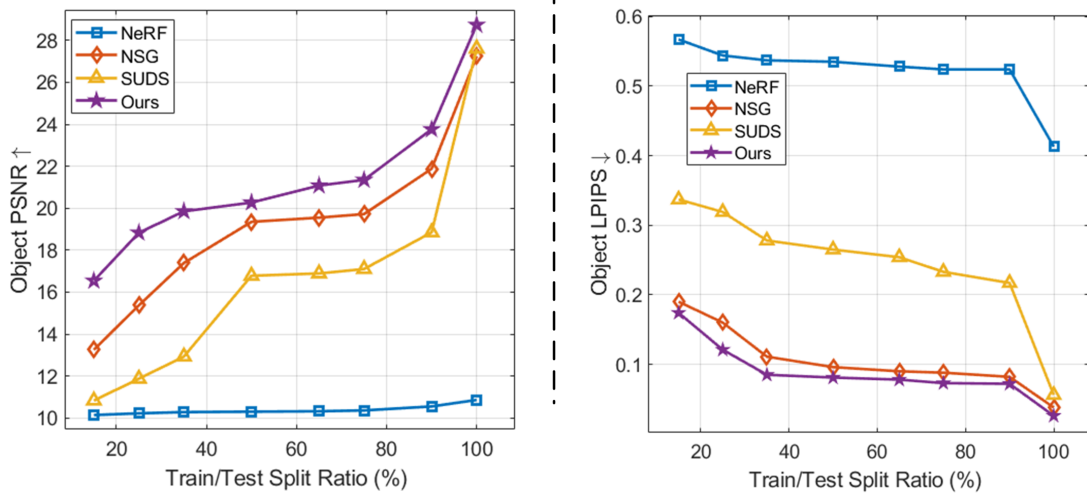


Fig. 6 Dynamic objects view synthesis evaluation: measures of image fidelity plotted against train/test split ratio.

intersecting rays to generate sampling points for the static background. In our experiment we use 10 to 32 planes to capture different movement scenarios and camera perspectives.

Ray-Box Sampling. For each ray r in the dynamic object node, we use the ray-box sampling method. We check the rays that intersect with the dynamic object nodes and translate them to the object coordinate space. Then, we apply the efficient AABB intersection method [26] to compute all ray-box entrance and exit points (t_{o1}, t_{oN}) . We stratified sample points x_o between the entrance and exit points:

$$t_{on} = \frac{n-1}{N_d-1} (t_{oN} - t_{o1}) + t_{o1} \quad (9)$$

Ray-Box Intersection involves transforming rays into local frames of dynamic objects, enabling computation of intersections within scaled axis-aligned bounding boxes (AABBs), as shown in Fig. 4. Equidistant quadrature points along the rays within the bounding box are sampled to represent object surfaces accurately. Experimentally, using 7 equidistant points per ray and object node was found to balance accuracy and rendering speed.

Volume Rendering. The sample points along the rays can be represented as: $\{t_i\}_{i=1}^{N_s+m_j N_d}$. m_o represents the number of dynamic nodes that the ray intersects along its path. The color $c(x_i)$ and volumetric density $\sigma(x_i)$ of each intersection point is predicted from the respective network in the static background node $F_{\theta_{bg}}$ or dynamic objects node F_{θ_o} . Then, we define the termination probability

and color as:

$$\hat{\mathbf{C}}(\mathbf{x}) = \sum_{i=1}^{N_s+m_j N_d} T_i \alpha_i \mathbf{c}_i, \hat{\mathbf{D}}(\mathbf{x}) = \sum_{i=1}^{N_s+m_j N_d} T_i \alpha_i \delta_i \quad (10)$$

$$T_i = \exp\left(-\sum_{k=1}^{i-1} \sigma_k \delta_k\right), \alpha_i = 1 - \exp(-\sigma_i \delta_i) \quad (11)$$

where $\delta_i = t_{i+1} - t_i$ is the distance between adjacent points.

3.5 Progressive Scene Graph Joint Learning

For the large-scale dynamic scene, we divide the entire scene into multi-local scene graphs. Whenever the camera moves to the bound of the current scene graph, we dynamically initialize a new neural scene graph and stop optimizing the previous ones.

When encountering the same objects observed in two local scenes, we update only the dynamic object network in the current scene graph because the optimization of the previous scene graphs is frozen. To mitigate potential quality reduction in the former scene graph caused by this strategy, each subset contains some overlapping images, essential for achieving consistent reconstructions in the global scene. We also dynamically adjust local scene bounds during optimization. This helps prevent the undesired splitting of dynamic elements and optimizes the overall reconstruction process.

In each local scene graph, we use color loss to optimize the representation model for the background and dynamic object node:

$$\mathcal{L}_c = \frac{1}{N} \sum_{i=1}^N (\hat{\mathbf{C}}_i - \mathbf{C}_i)^2 \quad (12)$$

In addition, we propose a lidar points projection loss to supervise our rendering depth and enhance the geometry consistency:

$$\mathcal{L}_d = \frac{1}{|R_i|} \sum_{i \in R_i} (\hat{\mathbf{D}}_i - \Pi(P, \{R, t\}, K))^2 \quad (13)$$

where $\Pi()$ is the projection from 3D point P_i to the depth of 2D pixel. R_i is the set of rays with a valid depth projection value. Inspired by [9], we

also use ray distribution loss to minimize the KL divergence between the rendered ray distribution $h(t)$ and the noisy depth distribution:

$$\mathcal{L}_\sigma = \sum_i \log h_i \exp\left(-\frac{(t_i - \hat{\mathbf{D}}_i)^2}{2\hat{\sigma}_i^2}\right) \delta_i \quad (14)$$

where $\hat{\sigma}_i^2$ is the variance of depth D_i .

Far-Field Modeling (Sky). Outdoor scenes contain sky regions where rays never intersect any opaque surfaces, and thus, the NeRF model gets a weak supervisory signal in those regions.

To modulate which rays utilize the environment map, we run the segment anything model (SAM) for each image to detect pixels of the sky: $S_i = S(I_i)$, where $S_i(r) = 1$ if the ray r goes through a sky pixel in image i . We then design a far-field loss to encourage at all point samples along rays through sky pixels to have zero density:

$$\mathcal{L}_{\text{seg}} = \mathbb{E}_{\mathbf{r} \sim I_i} \left[S_i(\mathbf{r}) \int_{t_n}^{t_f} (T \cdot \alpha)^2 dt \right] \quad (15)$$

At each step, the gradient at each trainable node in L and F intersecting with the rays is computed and backpropagated.

4 Implementation

4.1 Dataset and Metrics

We evaluate ProSGNeRF on KITTI tracking datasets [18] for the real-world urban scene. The KITTI dataset [18] is captured using a stereo camera. Each sequence consists of more than 100 time steps and images of size 1242×375 , each from two camera perspectives and more than 12 dynamic objects from different classes. We strictly follow the experimental setting of NSG and SUDS to ensure fairness. In addition to the experiments on the KITTI dataset, we further conducted evaluations on the synthetic vKITTI2 dataset [3] and the larger real-world Waymo dataset [37] and nuScenes [4] datasets, thereby demonstrating the outstanding performance of our model across diverse scenarios and ensuring a comprehensive evaluation. We report the standard view synthesis metrics PSNR, SSIM, and LPIPS scores for all evaluations.

Dataset Generation We construct a new dataset using the pre-trained SAM2 model and a 3D object detection model, which contains camera intrinsics

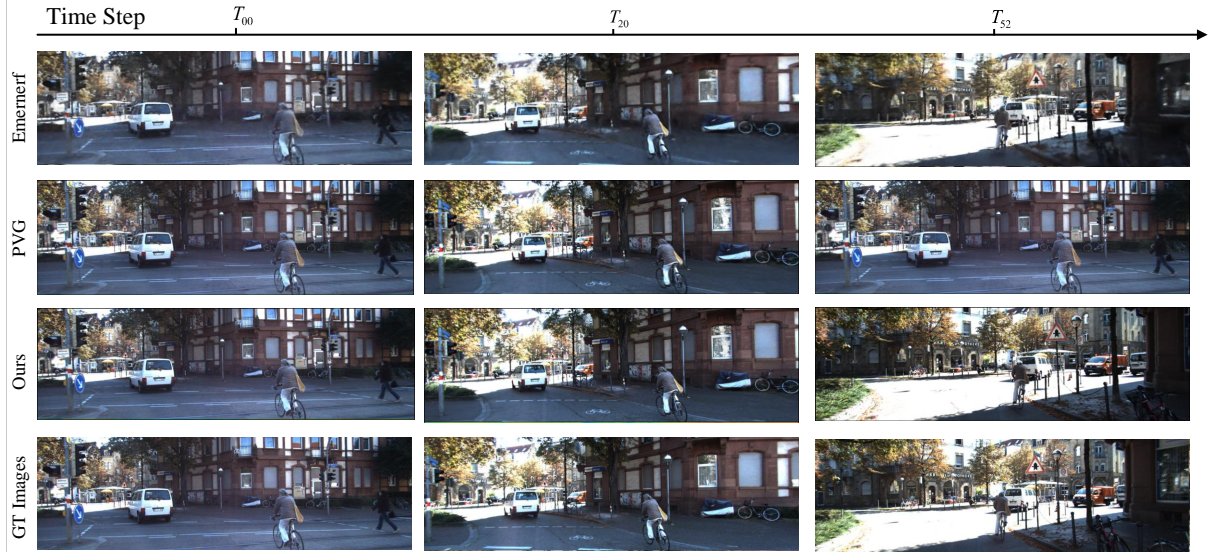


Fig. 7 We also present our method for novel view synthesis performance on the KITTI 0000 sequence, with high-dynamic human. The results clearly show that our approach achieve high accuracy reconstruction performance.

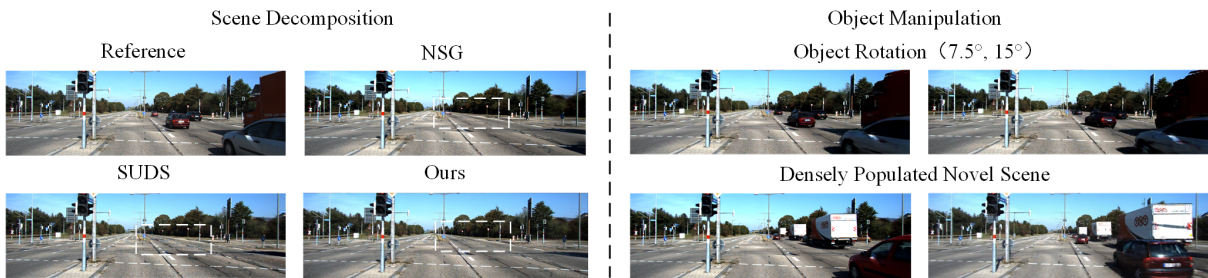


Fig. 8 Scene decomposition and object manipulation. We demonstrate the decomposition capability of our progressive scene graph compared to other methods, emphasizing its capacity to isolate foreground objects and generate cleaner backgrounds. Additionally, the right part showcases our proficiency in scene editing, depicting our capability to render rotated objects and synthesize densely populated novel scenes realistically.

and extrinsics, RGB images, as well as 3D bounding boxes and 2D masks of objects. We use SAM2 to acquire precise 2D semantic masks without the requirement for human annotation. Leveraging the promptable segmentation method, SAM predicts masks for both dynamic objects and scenarios in far-field situations. This approach enables the construction of a progressive neural scene graph, integrating instance masks from SAM and 3D bounding boxes derived from machine predictions.

4.2 Parameters

ProSGNeRF is evaluated on a desktop PC with NVIDIA A100 GPU. For experimental settings.

Each decoder uses the five fully-connected residual blocks. The bounding box dimensions are scaled to include the shadows for better reconstruction.

Loss weight In refining local scene graphs, we utilize a color loss mechanism to enhance the representation of background and dynamic object nodes. Introducing a novel lidar points projection loss bolsters geometric consistency by supervising rendering depth. Drawing inspiration from [9], our approach incorporates a ray distribution loss to minimize divergence between the rendered ray distribution $h(t)$ and observed noisy depth distribution. Moreover, we introduce a far-field loss function to ensure zero density for point samples

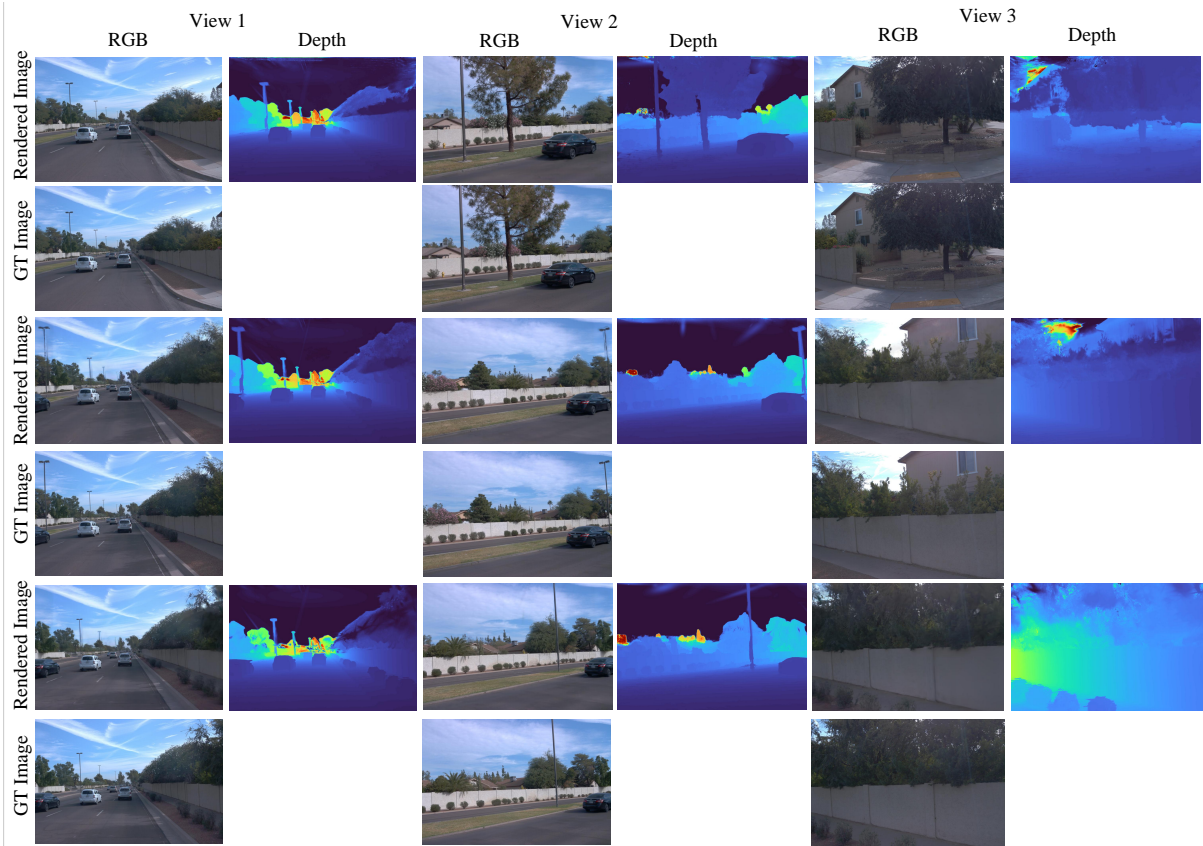


Fig. 9 We also present our method for scene reconstruction performance. The results clearly show that our approach achieve high accuracy reconstruction performance.

along rays passing through sky pixels. The depth loss and KL divergence loss are pivotal in maintaining geometric consistency, ultimately enhancing scene accuracy and geometry portrayal. However, excessive emphasis on these losses can negatively impact image metrics. Hence, controlling their weights is crucial for optimal performance.

In our experiments, We set $\lambda_c = 1$, $\lambda_d = 0.005$, $\lambda_\sigma = 0.005$, $\lambda_{seg} = 0.001$. These adjustments strike a balance between geometric accuracy and image fidelity, refining scene representation while minimizing adverse effects on image-related metrics.

Baseline We compare our method against state-of-art implicit neural rendering methods: the original NeRF implementation [29], NeRF+Time, NSG [32], SUDS [40], S-NeRF [45], StreetSurf [19], MARS [42], EmerNeRF [47], and 3D Gaussian Splatting [21], StreetGaussian [46], Driving Gaussian [51], PVG [8], DeSiRe-GS [35].

5 Experiments

In this section, we validate the proposed ProSGN-eRF method on the existing autonomous driving datasets KITTI [18], VKITTI [3], Waymo [37] and nuScenes datasets [4]. We validate that our method outperforms existing dynamic representation methods in image reconstruction, novel view synthesis, and dynamic object manipulation.

5.1 Experimental Results

Image Reconstruction and Novel View Synthesis. We conduct image reconstruction and novel view synthesis experiments in urban dynamic scenes. Table 3 reports the qualitative results of image reconstruction and novel view synthesis on the KITTI dataset [18]. To comprehensively evaluate performance under varying data availability, we adopt multiple train and test splits, including using the full dataset, holding out every fourth time step, holding out every other time

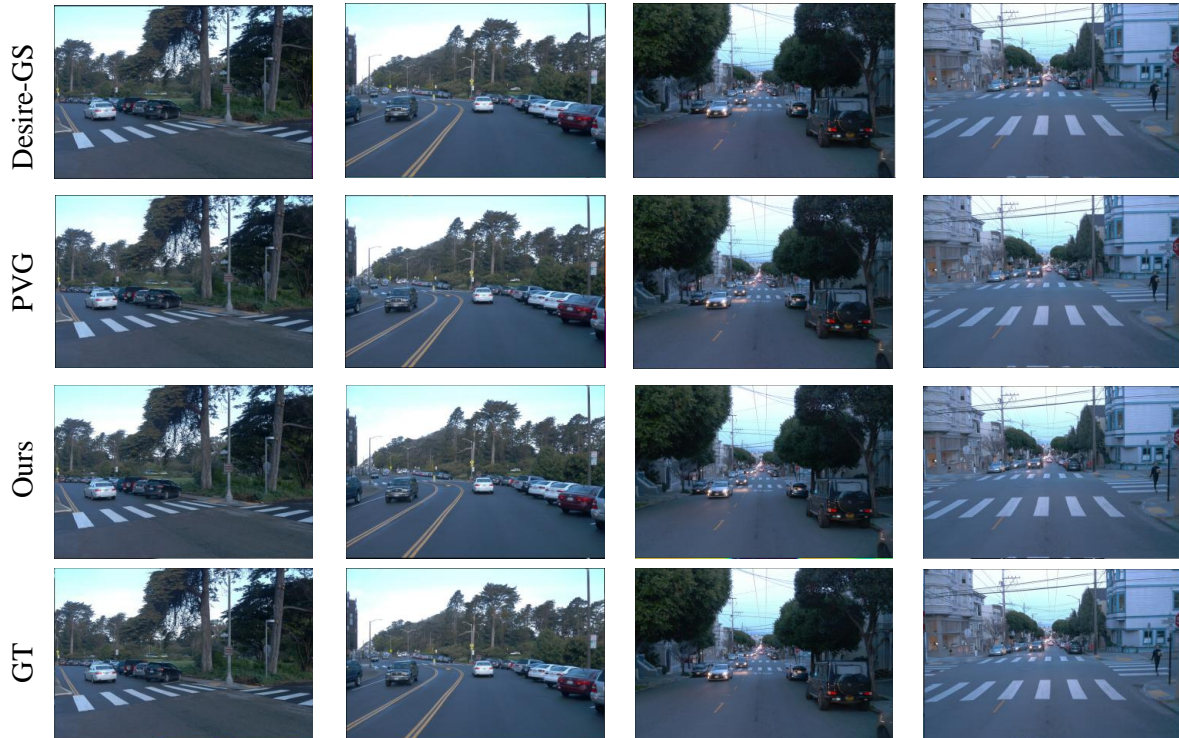


Fig. 10 We also present our method for scene reconstruction performance on the Waymo dataset [37], compared with PVG and Desire-gs. The results clearly show that our approach achieve high accuracy reconstruction performance.

Table 5 Reconstruction performance on Waymo [37] dataset. We outperform other works on image reconstruction and novel view synthesis.

Methods	Waymo [37]					
	Image Reconstruction			Novel View Synthesis		
	PSNR \uparrow	SSIM \uparrow	LPIPS \downarrow	PSNR \uparrow	SSIM \uparrow	LPIPS \downarrow
NeRF [29]	18.89	0.515	0.398	18.45	0.508	0.405
NSG [32]	24.08	0.656	0.441	21.05	0.575	0.487
SUDS [40]	28.83	0.805	0.317	25.36	0.783	0.384
S-NeRF [45]	19.67	0.528	0.387	19.25	0.517	0.402
StreetSurf [19]	26.73	0.849	0.372	23.79	0.825	0.401
3DGS [21]	27.99	0.866	0.293	25.08	0.822	0.319
MARS [42]	21.84	0.682	0.431	20.69	0.637	0.453
EmerNeRF [47]	28.11	0.784	0.375	25.94	0.765	0.383
PVG [8]	31.45	0.897	0.243	27.49	0.838	0.303
DeSiRe-GS [35]	31.89	0.904	0.238	28.84	0.842	0.300
Ours	32.55	0.912	0.235	29.89	0.861	0.275

step, and training with only one out of every four time steps. Quantitative evaluations are performed using PSNR, SSIM, and LPIPS metrics. Across all experimental settings, the proposed method consistently outperforms all baseline approaches

on all evaluation metrics. Compared with NeRF based methods, our approach achieves substantially improved performance in both background reconstruction and dynamic object reconstruction.

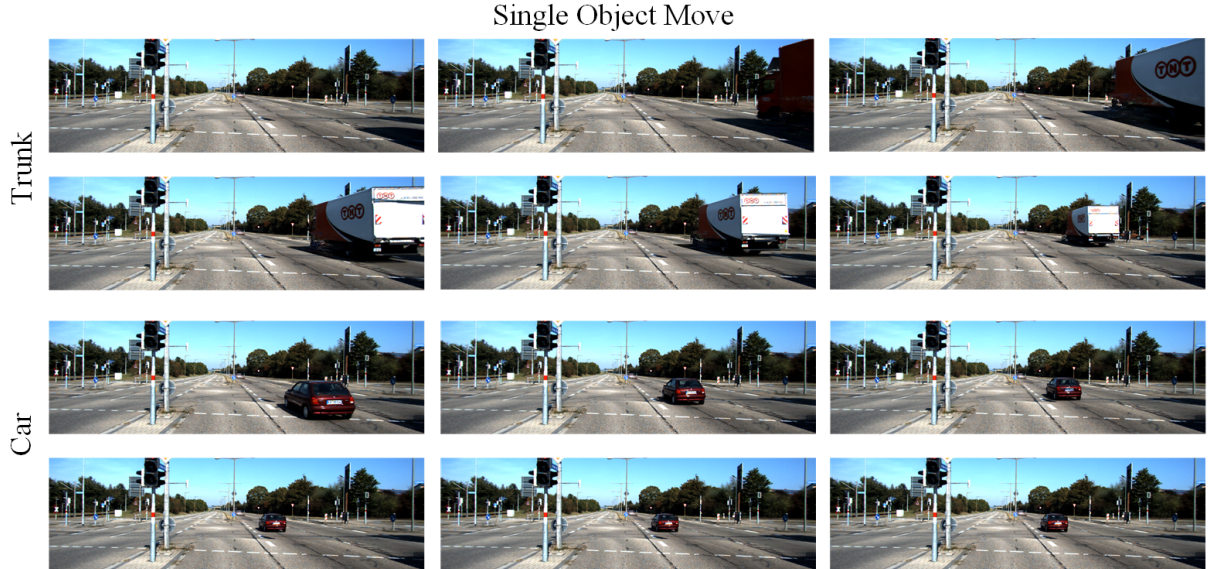


Fig. 11 We illustrate the scene editing results for the single object movement setting. As shown in the figure, our method enables flexible insertion of different types of vehicles into the scene, including trucks and cars.

Table 6 Quantitative comparison with existing methods on the nuScenes dataset [4]. We report PSNR, SSIM, and LPIPS. Higher PSNR and SSIM indicate better performance, while lower LPIPS is better.

Methods	PSNR \uparrow	SSIM \uparrow	LPIPS \downarrow
Instant-NGP [31]	16.78	0.519	0.570
NeRF+Time	17.54	0.565	0.532
NSG [32]	21.67	0.671	0.424
Mip-NeRF [1]	18.08	0.572	0.551
Mip-NeRF360 [2]	22.61	0.688	0.395
Urban-NeRF [36]	20.75	0.627	0.480
S-NeRF [45]	25.43	0.730	0.302
SUDS [40]	21.26	0.603	0.466
EmerNeRF [47]	26.75	0.760	0.311
3DGS [21]	26.08	0.717	0.298
4DGS [41]	19.79	0.622	0.473
DrivingGaussian [51]	28.74	0.865	0.237
Ours	29.24	0.878	0.223

This improvement can be attributed to the progressive scene graph design, which enables large-scale ego-motion scene modeling, as well as the incorporation of multiresolution hash encoding in the background network, allowing more accurate representation of fine scale geometric and texture details. In comparison with 3DGS based methods, our approach demonstrates superior performance in dynamic object reconstruction and exhibits stronger generalization capability. Specifically, our method is able to effectively model a wide range of

dynamic object categories across different scenes, highlighting its robustness and adaptability in complex dynamic environments. In particular, as the number of available training views decreases, our method exhibits a more significant advantage in novel view synthesis performance.

In addition to KITTI, we also present image reconstruction and novel view synthesis results on the VKITTI [3], Waymo [37], and nuScenes [4] datasets in Tab. 3, Tab. 4, Tab. 5, and Tab. 6. The experimental results across these diverse urban driving benchmarks clearly demonstrate the effectiveness and strong generalization capability of the proposed method, showing its ability to accurately model both static background structures and dynamic objects in complex real world scenes. The qualitative results are shown in Fig. 5 and 7. Figure 5 depicts the appearance of the dynamic scene at different time instances from left to right (time step: 66, 80, 102, 234). The vanilla NeRF implicit rendering fails to reconstruct dynamic scenes accurately. It can only represent static scenes, which leads to nearly identically rendered frames for all the sequences. The NSG algorithm provides a relatively accurate representation of dynamic objects but cannot handle scenes with large-scale camera ego-motion. This limitation arises from the fixed root of their scene graph representation, which cannot move with the camera. In the last column of the

figure, their reconstruction results appear highly blurred when the camera moves. SUDS exhibits poor representation capability for dynamic objects; their objects appear blurry in Fig. 5. Methods based on 3DGS achieve relatively high accuracy in background modeling. However, they exhibit limited performance in dynamic object reconstruction, suffer from poor generalization capability, and rely heavily on high precision point cloud initialization such as LiDAR measurements. In contrast, our method leverages prior knowledge encoded in a foundation model to guide scene understanding, enabling effective extraction of object appearance and shape features. This design allows the proposed approach to robustly handle the sparse observation problem caused by high speed object motion, while simultaneously maintaining strong generalization performance across different scenes and object categories. Especially as the number of training views decreases, all the existing methods generate ghosting artifacts near areas of movement. We also present object PSNR and LPIPS curves as the training view falls in Fig. 6. ProS-GNeRF achieves state of the art performance in dynamic object reconstruction and novel view synthesis under large scale camera ego motion, which strongly validates the effectiveness of the proposed frequency modulated foundation model design.

Scene Decomposition and Object Manipulation. Compared to other methods, our approach excels significantly in its ability for scene decomposition and object manipulation. The structure of the proposed method can naturally decompose scenes into dynamic and static scene components. We present the rendering of isolated nodes of our progressive scene graph in Fig. 8 and Fig. 9 to present the scene editing ability. In Fig. 8, we compared the scene decomposition ability of our method and other methods. We can see that our method learns a clean decomposition between the objects and the background.

We then generate previously unseen frames of novel object arrangements, temporal variations. Our progressive neural scene graph architecture allows dynamic urban scene editing, which can be manipulated at its edges and nodes. To demonstrate the flexibility of the proposed scene representation, we rotate the pose of dynamic objects. We present the view synthesis results in Fig. 8 and Fig. 11. Note that we have not observed the rotation of dynamic objects during training.

In addition to object manipulation and node removal of the dynamic objects, our method allows for constructing completely novel scene graphs and novel view synthesis. Fig. 8 shows view synthesis results that we randomly insert new object nodes and new object positions with new transformations. We constrain samples to the joint set of all observed road trajectories. Note that all these translations and manipulations have not been observed during training. Figure 11 illustrates the scene editing results for the single object movement setting. As shown in the figure, our method enables flexible insertion of different types of vehicles into the scene, including trucks and cars. These results demonstrate the strong object level editability of the proposed approach and highlight the advantages of the scene graph structure in supporting controllable and semantically consistent scene manipulation.

5.2 Ablation Study

In this section, we provide more detailed ablation studies of our method. The detailed experimental results is shown in Tab. 7. The table presents an ablation study showing the impact of different design choices on the performance of a scene representation model. It evaluates image reconstruction and novel view synthesis on the KITTI dataset across three metrics: PSNR, SSIM, and LPIPS.

Several variants of the model are compared by incrementally removing or changing components. This includes ablations of the progressive scene graph, loss functions, encoder sharing schemes, input modalities, and sampling strategies. The bottom row shows results for the full model with all components enabled.

The full model with all features performs the best across most evaluation metrics. The most impactful design choices are the progressive scene graph, separate encoders for shape and appearance, and ray-based sampling. Removing or changing these degrades performance, demonstrating their importance. Other ablations produce smaller differences, suggesting less critical roles. Moreover, we present the ablation study on progressive scene representation with pre-dividing in Tab. 8.

Overall, the ablation quantitatively validates design decisions through comparative analysis. It highlights key model architectures and training techniques that boost reconstruction fidelity and

Table 7 Ablation study of our design choices on the full 0006 sequence of KITTI datasets [18] for image reconstruction and 50% for novel view synthesis. The metrics are PSNR, SSIM, LPIPS.

Methods	Image Reconstruction			Novel View Synthesis-50%		
	PSNR \uparrow	SSIM \uparrow	LPIPS \downarrow	PSNR \uparrow	SSIM \uparrow	LPIPS \downarrow
w/o progressive scene graph	26.34	0.849	0.079	23.98	0.795	0.137
w/o overlapping between local scene graph	28.79	0.862	0.065	24.98	0.834	0.103
with only MLP	28.75	0.865	0.065	24.81	0.832	0.104
with only Dino v2	29.41	0.881	0.060	25.98	0.865	0.088
with frequency modulation and MLP	27.18	0.860	0.068	24.72	0.831	0.105
w/o object pose input	27.98	0.864	0.071	24.75	0.822	0.103
with shared encoders for shape and appearance	27.15	0.867	0.073	24.28	0.816	0.113
using the shared network for car and truck	27.81	0.877	0.071	24.56	0.839	0.101
w/o depth loss	29.25	0.885	0.063	25.19	0.865	0.094
w/o KL divergence loss	29.28	0.891	0.069	25.45	0.860	0.096
w/o far-field loss	29.37	0.890	0.067	25.28	0.862	0.095
without planes sampling	29.68	0.896	0.065	25.89	0.864	0.091
without ray-box sampling	29.72	0.897	0.063	25.82	0.865	0.090
Full Model	30.31	0.931	0.057	26.55	0.878	0.086

view synthesis photorealism. The table effectively summarizes component importance across multiple metrics.

Table 8 Ablation study on KITTI [18] and Waymo [37] datasets. We demonstrate the effectiveness of progressive scene representation and online scaling.

Methods	KITTI [18]			Waymo [37]		
	PSNR	SSIM	LPIPS	PSNR	SSIM	LPIPS
pre-divide	24.89	0.827	0.118	31.28	0.908	0.112
w/o scaling	25.29	0.837	0.108	32.85	0.915	0.103
Ours	25.95	0.856	0.095	33.80	0.931	0.092

Progressive scene graph. We use the original neural scene graph instead of our progressive scene graph, which leads to a remarkable decrease in the image accuracy metrics in dynamic urban scenes with large-scale camera ego-motion.

Frequency modulated foundation model. In the second experiment, we replace our frequency foundation model with the original MLP. We can see that the network cannot effectively represent dynamic objects due to the sparsity and movement of dynamic objects.

Loss. In the third and fourth experiments, we remove the depth loss and KL divergence loss from our network and compare it to the full model. The comparison indicates that the depth loss and KL divergence loss provide the geometry consistency of the scene representation, improving the scene’s accuracy and geometry representation. The full model achieves the best image reconstruction and novel view synthesis performance.

6 Conclusion

We present the first approach that tackles the challenge of representing multi-dynamic object scenes with large-scale camera ego-motion. A progressive neural scene graph method is proposed, which learns a graph-structured and spatial representation of multiple dynamic and static scene elements. Our method dynamically instantiates local scene graphs and decomposes the entire scene into multiple local scene graphs, significantly improving the representation ability for large-scale scenes. For dynamic objects, our frequency auto-encoder network efficiently encodes shape and appearance, addressing sparse view observations through frequency modulation. Extensive experiments on both simulated and real data achieve photo-realistic quality, showcasing the effectiveness of our approach. We believe that this work opens up the field of neural rendering for city-scale dynamic scene reconstruction.

Availability of data and materials All the datasets used in the paper will be publicly available.

References

- [1] Jonathan T Barron, Ben Mildenhall, Matthew Tancik, Peter Hedman, Ricardo Martin-Brualla, and Pratul P Srinivasan. Mip-nerf: A multiscale representation for anti-aliasing neural radiance fields. In *Proceedings of the IEEE/CVF International Conference on*

- Computer Vision*, pages 5855–5864, 2021.
- [2] Jonathan T Barron, Ben Mildenhall, Dor Verbin, Pratul P Srinivasan, and Peter Hedman. Mip-nerf 360: Unbounded anti-aliased neural radiance fields. In *Proceedings of the IEEE/CVF Conference on Computer Vision and Pattern Recognition*, pages 5470–5479, 2022.
 - [3] Johann Cabon, Naila Murray, and Martin Humenberger. Virtual kitti 2. *arXiv preprint arXiv:2001.10773*, 2020.
 - [4] Holger Caesar, Varun Bankiti, Alex H Lang, Sourabh Vora, Venice Erin Liong, Qiang Xu, Anush Krishnan, Yu Pan, Giancarlo Baldan, and Oscar Beijbom. nuscenes: A multimodal dataset for autonomous driving. In *Proceedings of the IEEE/CVF conference on computer vision and pattern recognition*, pages 11621–11631, 2020.
 - [5] Mathilde Caron, Hugo Touvron, Ishan Misra, Hervé Jégou, Julien Mairal, Piotr Bojanowski, and Armand Joulin. Emerging properties in self-supervised vision transformers. In *Proceedings of the IEEE/CVF international conference on computer vision*, pages 9650–9660, 2021.
 - [6] Jiazhong Cen, Jiemin Fang, Zanwei Zhou, Chen Yang, Lingxi Xie, Xiaopeng Zhang, Wei Shen, and Qi Tian. Segment anything in 3d with radiance fields. *International Journal of Computer Vision*, pages 1–23, 2025.
 - [7] Minglin Chen, Longguang Wang, Yinjie Lei, Zilong Dong, and Yulan Guo. Learning spherical radiance field for efficient 360° unbounded novel view synthesis. *IEEE Transactions on Image Processing*, 33:3722–3734, 2024.
 - [8] Yurui Chen, Chun Gu, Junzhe Jiang, Xiaotian Zhu, and Li Zhang. Periodic vibration gaussian: Dynamic urban scene reconstruction and real-time rendering. *arXiv preprint arXiv:2311.18561*, 2023.
 - [9] Kangle Deng, Andrew Liu, Jun-Yan Zhu, and Deva Ramanan. Depth-supervised nerf: Fewer views and faster training for free. In *Proceedings of the IEEE/CVF Conference on Computer Vision and Pattern Recognition (CVPR)*, pages 12882–12891, June 2022.
 - [10] Tianchen Deng, Xuefeng Chen, Yi Chen, Qu Chen, Yuyao Xu, Lijin Yang, Le Xu, Yu Zhang, Bo Zhang, Wuxiong Huang, and Hesheng Wang. Gaussiandwm: 3d gaussian driving world model for unified scene understanding and multi-modal generation. *arXiv preprint arXiv:2512.23180*, 2025.
 - [11] Tianchen Deng, Guole Shen, Xun Chen, Shenghai Yuan, Hongming Shen, Guohao Peng, Zhenyu Wu, Jingchuan Wang, Lihua Xie, Danwei Wang, Hesheng Wang, and Weidong Chen. Mcn-slam: Multi-agent collaborative neural slam with hybrid implicit neural scene representation. *arXiv preprint arXiv:2506.18678*, 2025.
 - [12] Tianchen Deng, Guole Shen, Tong Qin, Jianyu Wang, Wentao Zhao, Jingchuan Wang, Danwei Wang, and Weidong Chen. Plgslam: Progressive neural scene representation with local to global bundle adjustment. In *Proceedings of the IEEE/CVF Conference on Computer Vision and Pattern Recognition (CVPR)*, pages 19657–19666, June 2024.
 - [13] Tianchen Deng, Guole Shen, Chen Xun, Shenghai Yuan, Tongxin Jin, Hongming Shen, Yanbo Wang, Jingchuan Wang, Hesheng Wang, Danwei Wang, et al. Mne-slam: Multi-agent neural slam for mobile robots. In *Proceedings of the Computer Vision and Pattern Recognition Conference*, pages 1485–1494, 2025.
 - [14] Tianchen Deng, Nailin Wang, Chongdi Wang, Shenghai Yuan, Jingchuan Wang, Hesheng Wang, Danwei Wang, and Weidong Chen. Incremental joint learning of depth, pose and implicit scene representation on monocular camera in large-scale scenes. *IEEE Transactions on Automation Science and Engineering*, pages 1–1, 2025.
 - [15] Tianchen Deng, Wenhua Wu, Junjie He, Yue Pan, Xirui Jiang, Shenghai Yuan, Danwei Wang, Hesheng Wang, and Weidong Chen. Vpgs-slam: Voxel-based progressive 3d gaussian slam in large-scale scenes. *arXiv preprint arXiv:2505.18992*, 2025.
 - [16] Xiao Fu, Shangzhan Zhang, Tianrun Chen, Yichong Lu, Lanyun Zhu, Xiaowei Zhou, Andreas Geiger, and Yiyi Liao. Panoptic nerf: 3d-to-2d label transfer for panoptic urban scene segmentation. In *2022 International Conference on 3D Vision (3DV)*, pages 1–11. IEEE, 2022.
 - [17] Chen Gao, Ayush Saraf, Johannes Kopf, and Jia-Bin Huang. Dynamic view synthesis from dynamic monocular video. In *Proceedings of*

- the *IEEE/CVF International Conference on Computer Vision*, pages 5712–5721, 2021.
- [18] Andreas Geiger, Philip Lenz, Christoph Stiller, and Raquel Urtasun. Vision meets robotics: The kitti dataset. *The International Journal of Robotics Research*, 32(11):1231–1237, 2013.
- [19] Jianfei Guo, Nianchen Deng, Xinyang Li, Yeqi Bai, Botian Shi, Chiyu Wang, Chenjing Ding, Dongliang Wang, and Yikang Li. Street-surf: Extending multi-view implicit surface reconstruction to street views. *arXiv preprint arXiv:2306.04988*, 2023.
- [20] Chenxi Huang, Yuenan Hou, Weicai Ye, Di Huang, Xiaoshui Huang, Binbin Lin, and Deng Cai. Nerf-det++: Incorporating semantic cues and perspective-aware depth supervision for indoor multi-view 3d detection. *IEEE Transactions on Image Processing*, 34:2575–2587, 2025.
- [21] Bernhard Kerbl, Georgios Kopanas, Thomas Leimkühler, and George Drettakis. 3d gaussian splatting for real-time radiance field rendering. *ACM Trans. Graph.*, 42(4):139–1, 2023.
- [22] Alexander Kirillov, Eric Mintun, Nikhila Ravi, Hanzi Mao, Chloe Rolland, Laura Gustafson, Tete Xiao, Spencer Whitehead, Alexander C Berg, Wan-Yen Lo, et al. Segment anything. *arXiv preprint arXiv:2304.02643*, 2023.
- [23] Abhijit Kundu, Kyle Genova, Xiaoqi Yin, Alireza Fathi, Caroline Pantofaru, Leonidas J Guibas, Andrea Tagliasacchi, Frank Dellaert, and Thomas Funkhouser. Panoptic neural fields: A semantic object-aware neural scene representation. In *Proceedings of the IEEE/CVF Conference on Computer Vision and Pattern Recognition*, pages 12871–12881, 2022.
- [24] Tianye Li, Mira Slavcheva, Michael Zollhoefer, Simon Green, Christoph Lassner, Changil Kim, Tanner Schmidt, Steven Lovegrove, Michael Goesele, Richard Newcombe, et al. Neural 3d video synthesis from multi-view video. In *Proceedings of the IEEE/CVF Conference on Computer Vision and Pattern Recognition*, pages 5521–5531, 2022.
- [25] Zhengqi Li, Simon Niklaus, Noah Snavely, and Oliver Wang. Neural scene flow fields for space-time view synthesis of dynamic scenes. In *Proceedings of the IEEE/CVF Conference on Computer Vision and Pattern Recognition*, pages 6498–6508, 2021.
- [26] Alexander Majercik, Cyril Crassin, Peter Shirley, and Morgan McGuire. A ray-box intersection algorithm and efficient dynamic voxel rendering. *Journal of Computer Graphics Techniques Vol.*, 7(3):66–81, 2018.
- [27] Ricardo Martin-Brualla, Noha Radwan, Mehdi SM Sajjadi, Jonathan T Barron, Alexey Dosovitskiy, and Daniel Duckworth. Nerf in the wild: Neural radiance fields for unconstrained photo collections. In *Proceedings of the IEEE/CVF Conference on Computer Vision and Pattern Recognition*, pages 7210–7219, 2021.
- [28] Andreas Meuleman, Yu-Lun Liu, Chen Gao, Jia-Bin Huang, Changil Kim, Min H Kim, and Johannes Kopf. Progressively optimized local radiance fields for robust view synthesis. In *Proceedings of the IEEE/CVF Conference on Computer Vision and Pattern Recognition*, pages 16539–16548, 2023.
- [29] Ben Mildenhall, Pratul P. Srinivasan, Matthew Tancik, Jonathan T. Barron, Ravi Ramamoorthi, and Ren Ng. Nerf: Representing scenes as neural radiance fields for view synthesis. In *European Conference on Computer Vision*, 2020.
- [30] Norman Müller, Andrea Simonelli, Lorenzo Porzi, Samuel Rota Buló, Matthias Nießner, and Peter Kotschieder. Autorf: Learning 3d object radiance fields from single view observations. In *Proceedings of the IEEE/CVF Conference on Computer Vision and Pattern Recognition*, pages 3971–3980, 2022.
- [31] Thomas Müller, Alex Evans, Christoph Schied, and Alexander Keller. Instant neural graphics primitives with a multiresolution hash encoding. *ACM transactions on graphics (TOG)*, 41(4):1–15, 2022.
- [32] Julian Ost, Fahim Mannan, Nils Thuerey, Julian Knodt, and Felix Heide. Neural scene graphs for dynamic scenes. In *Proceedings of the IEEE/CVF Conference on Computer Vision and Pattern Recognition*, pages 2856–2865, 2021.
- [33] Keunhong Park, Utkarsh Sinha, Jonathan T Barron, Sofien Bouaziz, Dan B Goldman, Steven M Seitz, and Ricardo Martin-Brualla. Nerfies: Deformable neural radiance fields.

- In *Proceedings of the IEEE/CVF International Conference on Computer Vision*, pages 5865–5874, 2021.
- [34] Keunhong Park, Utkarsh Sinha, Peter Hedman, Jonathan T Barron, Sofien Bouaziz, Dan B Goldman, Ricardo Martin-Brualla, and Steven M Seitz. Hypernerf: A higher-dimensional representation for topologically varying neural radiance fields. *arXiv preprint arXiv:2106.13228*, 2021.
- [35] Chensheng Peng, Chengwei Zhang, Yixiao Wang, Chenfeng Xu, Yichen Xie, Wenzhao Zheng, Kurt Keutzer, Masayoshi Tomizuka, and Wei Zhan. Desire-gs: 4d street gaussians for static-dynamic decomposition and surface reconstruction for urban driving scenes. In *Proceedings of the Computer Vision and Pattern Recognition Conference*, pages 6782–6791, 2025.
- [36] Konstantinos Rematas, Andrew Liu, Pratul P Srinivasan, Jonathan T Barron, Andrea Tagliasacchi, Thomas Funkhouser, and Vittorio Ferrari. Urban radiance fields. In *Proceedings of the IEEE/CVF Conference on Computer Vision and Pattern Recognition*, pages 12932–12942, 2022.
- [37] Pei Sun, Henrik Kretzschmar, Xerxes Dotiwalla, Aurelien Chouard, Vijaysai Patnaik, Paul Tsui, James Guo, Yin Zhou, Yuning Chai, Benjamin Caine, Vijay Vasudevan, Wei Han, Jiquan Ngiam, Hang Zhao, Aleksei Timofeev, Scott M. Ettinger, Maxim Krivokon, Amy Gao, Aditya Joshi, Yu Zhang, Jonathon Shlens, Zhifeng Chen, and Dragomir Anguelov. Scalability in perception for autonomous driving: Waymo open dataset. *2020 IEEE/CVF Conference on Computer Vision and Pattern Recognition (CVPR)*, pages 2443–2451, 2019.
- [38] Matthew Tancik, Vincent Casser, Xinchen Yan, Sabeek Pradhan, Ben Mildenhall, Pratul P. Srinivasan, Jonathan T. Barron, and Henrik Kretzschmar. Block-nerf: Scalable large scene neural view synthesis. In *Proceedings of the IEEE/CVF Conference on Computer Vision and Pattern Recognition (CVPR)*, pages 8248–8258, June 2022.
- [39] Haithem Turki, Deva Ramanan, and Mahadev Satyanarayanan. Mega-nerf: Scalable construction of large-scale nerfs for virtual fly-throughs. In *Proceedings of the IEEE/CVF Conference on Computer Vision and Pattern Recognition (CVPR)*, pages 12922–12931, June 2022.
- [40] Haithem Turki, Jason Y Zhang, Francesco Ferroni, and Deva Ramanan. Suds: Scalable urban dynamic scenes. In *Proceedings of the IEEE/CVF Conference on Computer Vision and Pattern Recognition*, pages 12375–12385, 2023.
- [41] Guanjun Wu, Taoran Yi, Jiemin Fang, Lingxi Xie, Xiaopeng Zhang, Wei Wei, Wenyu Liu, Qi Tian, and Xinggang Wang. 4d gaussian splatting for real-time dynamic scene rendering. In *Proceedings of the IEEE/CVF conference on computer vision and pattern recognition*, pages 20310–20320, 2024.
- [42] Zirui Wu, Tianyu Liu, Liyi Luo, Zhide Zhong, Jianteng Chen, Hongmin Xiao, Chao Hou, Haozhe Lou, Yuantao Chen, Runyi Yang, et al. Mars: An instance-aware, modular and realistic simulator for autonomous driving. In *CAAI International Conference on Artificial Intelligence*, pages 3–15. Springer, 2023.
- [43] Wenqi Xian, Jia-Bin Huang, Johannes Kopf, and Changil Kim. Space-time neural irradiance fields for free-viewpoint video. In *Proceedings of the IEEE/CVF Conference on Computer Vision and Pattern Recognition*, pages 9421–9431, 2021.
- [44] Yuanbo Xiangli, Linning Xu, Xingang Pan, Nanxuan Zhao, Anyi Rao, Christian Theobalt, Bo Dai, and Dahua Lin. Bungeenerf: Progressive neural radiance field for extreme multi-scale scene rendering. In *European conference on computer vision*, pages 106–122. Springer, 2022.
- [45] Ziyang Xie, Junge Zhang, Wenye Li, Feihu Zhang, and Li Zhang. S-nerf: Neural radiance fields for street views. *arXiv preprint arXiv:2303.00749*, 2023.
- [46] Yunzhi Yan, Haotong Lin, Chenxu Zhou, Weijie Wang, Haiyang Sun, Kun Zhan, Xianpeng Lang, Xiaowei Zhou, and Sida Peng. Street gaussians: Modeling dynamic urban scenes with gaussian splatting. In *European Conference on Computer Vision*, pages 156–173. Springer, 2024.

- [47] Jiawei Yang, Boris Ivanovic, Or Litany, Xinshuo Weng, Seung Wook Kim, Boyi Li, Tong Che, Danfei Xu, Sanja Fidler, Marco Pavone, et al. Emernerf: Emergent spatial-temporal scene decomposition via self-supervision. *arXiv preprint arXiv:2311.02077*, 2023.
- [48] Jiawei Yang, Marco Pavone, and Yue Wang. Freenerf: Improving few-shot neural rendering with free frequency regularization. In *Proceedings of the IEEE/CVF Conference on Computer Vision and Pattern Recognition*, pages 8254–8263, 2023.
- [49] Kai Zhang, Gernot Riegler, Noah Snavely, and Vladlen Koltun. Nerf++: Analyzing and improving neural radiance fields. *arXiv preprint arXiv:2010.07492*, 2020.
- [50] Xiaoyun Zheng, Liwei Liao, Jianbo Jiao, Feng Gao, and Ronggang Wang. Surface-sos: Self-supervised object segmentation via neural surface representation. *IEEE Transactions on Image Processing*, 33:2018–2031, 2024.
- [51] Xiaoyu Zhou, Zhiwei Lin, Xiaojun Shan, Yongtao Wang, Deqing Sun, and Ming-Hsuan Yang. Drivinggaussian: Composite gaussian splatting for surrounding dynamic autonomous driving scenes. In *Proceedings of the IEEE/CVF conference on computer vision and pattern recognition*, pages 21634–21643, 2024.
- [52] Xingxing Zuo, Pouya Samangouei, Yunwen Zhou, Yan Di, and Mingyang Li. Fmgs: Foundation model embedded 3d gaussian splatting for holistic 3d scene understanding. *International Journal of Computer Vision*, 133(2):611–627, 2025.